



Computational analysis of thermo-mechanical characteristics in refill FSSW of thin AA7075-T6 sheets using smoothed-particle hydrodynamics

Venkata Somi Reddy Janga¹ · Mokhtar Awang¹ · Nabihah Sallih¹ · Chan Ray Mun² · Eng Ban Wee²

Received: 22 May 2023 / Revised: 1 September 2023 / Accepted: 18 September 2023 / Published online: 10 October 2023
© The Author(s) under exclusive licence to OWZ 2023

Abstract

A 3D thermo-mechanical model was developed employing the smoothed-particle hydrodynamics (SPH) technique to simulate the refill friction stir spot welding (refill FSSW) process and its tool plunging variants. SPH is a Lagrangian particle-based approach that can directly trace field variables' histories, handle large material deformations, and capture moving interfaces. These features of SPH make it appealing for the refill FSSW process, where the change of field variables is challenging to monitor experimentally. The numerical model of the shoulder-plunging variant (SP-refill FSSW) was validated by comparing results to experimental thermal data from the published literature. The temperatures correspond well with the experimental thermal data, and the model accurately predicted temperatures in the weld zone with an error of 0.52%. The thermal distribution, plastic strains, and material flow behaviours of the SP-refill FSSW and probe plunging variants (PP-refill FSSW) during the process are presented. The hook formation in connection with the material flow of the process is explained. The SPH numerical model can simulate refill FSSW, withstand severe deformations, and efficiently predict the field variables that help in a deeper understanding of the thermo-mechanical characteristics and joint formation in refill FSSW.

Keywords Smoothed-particle hydrodynamics · Refill friction stir spot welding · Thermo-mechanical analysis · Material flow · Friction stir spot welding · Simulation of solid-state joining processes

1 Introduction

Friction stir spot welding (FSSW) [1] is a potential substitute for heavier joining methods (bolts, rivets, etc.) and resistance spot welding [2]. The FSSW avoids many problems inherent in conventional welding of aluminium alloys (e.g., porosity and liquation cracking), and no additional weight is added, like rivets and bolts [2]. The FSSW technique involves a series of sequential actions, including the initial plunging motion, followed by a period of dwelling, and concluding with the retraction motion of the tool. FSSW was developed to join specific, inaccessible areas of the specimen but leaves a keyhole prone to corrosion and weakens the joint. The four fundamental types of FSSW approaches that are now in use are FSSW [1], refill FSSW [3], swept FSSW [4], and swing

FSSW [5]. The variants swing FSSW, swept FSSW, and refill FSSW are known to produce enhanced joint strengths and quality [6]. Studies show that the joint strength, particularly for dissimilar welds, can be improved by filler-added FSSW and Swept FSSW [7, 8]. Swept FSSW, although it produces enhanced joint strength and joint with a reduced keyhole, the keyhole/void is not entirely refilled. Refill FSSW [3], which produces a weld without a keyhole and improves joint strength, was developed by Helmholtz Zentrum Hereon. The tool-set (clamping ring, shoulder, and probe) is constructed in a way that the tools can move and rotate independently. The vertical movement sequence of the rotating tools allows us to classify the refill FSSW process as SP-refill FSSW/PP-refill FSSW variants [9]. Figure 1 depicts both the SP-refill FSSW and the PP-refill FSSW. In the initial/clamping stage, the specimens are held tightly by the action when the clamping ring is forced against the backing anvil. In the second stage for the SP-refill FSSW variant, the shoulder plunges into the specimens, and the probe moves in the opposite direction. The PP-refill FSSW variant plunges into the specimens, and the shoulder moves upwards. The specimen is

✉ Mokhtar Awang
mokhtar_awang@utp.edu.my

¹ Department of Mechanical Engineering, Universiti Teknologi PETRONAS, 32610 Seri Iskandar, Malaysia

² Altair Engineering Sdn Bhd, 50470 Kuala Lumpur, Malaysia

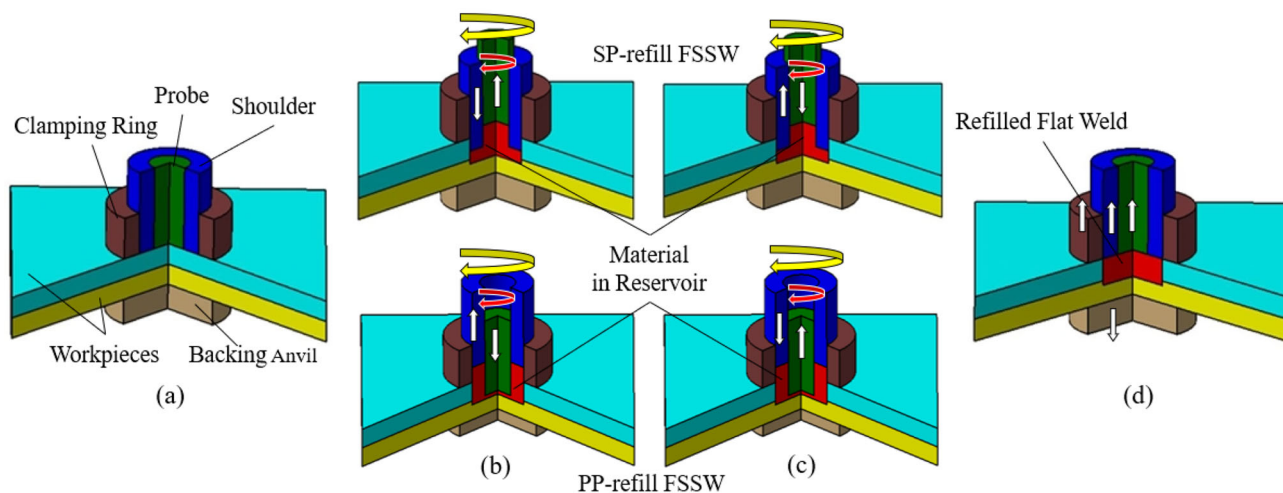


Fig. 1 Schematic representation of SP-refill FSSW and PP-refill FSSW. **a** Stage 1—Clamping; **b** Stage 2—Shoulder-Plunging/Probe Plunging; **c** Stage 3—Refilling; **d** Stage 4—Release

plasticized due to the frictional heat produced by the spinning shoulder/probe. In a sequential motion, the tools create a reservoir in which the displaced material is collected. In the refill stage, the direction of the rotating tools from the plunge stage is reversed, and the probe/shoulder pushes the softened material into the specimen. The force is released by the clamping ring in the finishing stage, leaving a refilled spot-welded specimen.

In a process like a refill FSSW, understanding the physics involved is crucial to optimize process variables and create high-strength welds. The majority of refill FSSW studies so far are concentrated on the experimental investigation of the SP-refill FSSW variant [10–13]. Cao et al. [14] compared SP-refill FSSW and pin-plunging reinforced refill FSSW for dissimilar alclad aluminium alloys. The presented results showed that pin plunging reinforced refill FSSW enhances joint strength by eliminating the voids and alclad concentration seen in SP-refill FSSW. Numerical analysis has been used extensively as an alternative to time-consuming and expensive experiments due to its ability to deliver accurate results during the entire process. To better understand the influence of various system attributes, a numerical model of refill FSSW can be used to simulate the effect of process parameters before any physical testing is performed. The compilation of various numerical modelling formulations and potential commercial software's is presented in a review by Marode et al. [15].

Only a few studies are available on the numerical modelling/simulation of the process. Muci-Küchler et al. [16] simulated the probe plunging process. The thermo-mechanical characteristics of only the probe plunge stage are presented using a numerical model developed in Abaqus/Explicit. Cao et al. [17] presented material flow and

hook formation during refill FSSW of AA6061-T6 specimens using a numerical model developed in Abaqus/Explicit. A Coupled Eulerian–Lagrangian (CEL) formulation is used for the model. The numerical model analyzed the material flow velocities in the process developed using Ansys-Fluent by Ji et al. [18]. However, the study does not report the material flow patterns and other quantitative results like thermal cycles. The thermal distribution, 2D material flow patterns, and joint formation in refill FSSW are analyzed by Kubit et al. [19] using a 2D numerical model built in Simufact. A CEL formulation in Abaqus/Explicit was utilized by Zhang et al. [20] to study the temperatures and material flow for joining AZ91D magnesium alloy specimens. Janga et al. [21, 22] developed a 3D thermo-mechanical model built on a Lagrangian-Incremental formulation in DEFORM-3D. The analysis of material flow patterns, strain, and thermal cycles during the refill FSSW of AA7075-T6 are presented. To model the refill FSSW in ForgeNxt3.2, Berger et al. [23] created an axisymmetric 2D model. Thermal results are used to verify the model, and the flow of materials is linked to the development of voids. Raza et al. [24] examined the evolution of intermetallic compounds (IMC) in dissimilar refill FSSW. The model is built in DEFORM-3D to predict temperatures and strains at weld locations, which are later used in a multi-phase model developed in PACE3D to predict the evolution of IMC.

The numerical models of the refill FSSW process so far are based on grid mesh techniques. Unlike grid-based approaches, SPH is a particle method (Lagrangian formulation) first developed for astrophysical simulations [25, 26]. In contrast to grid-based methods, SPH formulation can manage extreme deformations and mixing of materials without serious mesh distortion issues. SPH offers numerous advantages for modelling refill FSSW due to its Lagrangian

particle nature. First, it does not need front-tracking systems to describe complex interfaces and material flows, such as the merging/fusion and separation of the materials. Second, the Lagrangian framework permits precise solutions for momentum-dominated flows. Lastly, tracking the thermal cycles and deformation histories is easier for all Lagrangian volumes. In addition, the technique is Galilean invariant since the interactions between particles are determined by their respective locations and velocities. However, the SPH method's major drawback is the increased computational cost required to obtain accuracy compared to grid-based methods.

SPH approach was used by Tartakovsky et al. [27] to simulate friction stir welding (FSW). Although their study focussed on a 2D numerical modelling and fluid-based approach, they could predict the temperature and strain contours close to actual observations. Solid-based SPH was incorporated by Bhojwani [28] in LS-DYNA for FSW. Only the stress and strain results were shown here, and the material is modelled using Johnson–Cook constitutive law. Both the heat production and the thermal softening of the material were ignored. Using a 3D fluid-based SPH model, Pan et al. [29] were able to predict the field variables evolution that occurs during FSW. Fraser et al. [30] developed SPHfriction-3D code to simulate the FSW process to optimize parameters. Using an SPH-based numerical model developed in Abaqus, Ansari, and Behnagh [31] predicted the FSW temperatures and material flow in the plunge stage. Marode et al. [32] used Altair-RADIOSS to create a meshless SPH model of friction stir processing. Wormhole defects are discussed in relation to the material flow in the process.

Many earlier studies focussed on the experimental analysis of refill FSSW, and only a few studies are available on the numerical modelling of refill FSSW. The earlier studies' numerical models for refill FSSW were created using the grid-based approach. The main objective of this research is to develop a reliable mesh-free SPH-based numerical model to simulate and accurately predict and compare thermo-mechanical characteristics in the SP-refill FSSW and PP-refill FSSW variants. The model based on SPH can accurately predict and visualize the thermo-mechanical characteristics like temperatures, plasticization, material flow/joint formation, and defects during the process. To the authors' knowledge, this study is the first to develop a particle-based (SPH) mesh-free numerical model for simulating the refill FSSW. Also, no research was found focussing on the simulation of the PP-refill FSSW variant. The numerical temperature histories are compared with the experimental values from an earlier study. The obtained simulation findings are related to the experimental microstructure evolution and joint formation for a deeper insight into the refill FSSW process.

2 Numerical modelling: refill FSSW

The current study's numerical model of the SP-refill FSSW variant is developed based on experimental parameters such as material, process parameters, and tool geometry dimensions employed by Janga et al. [22]. Several issues have been tackled with the use of the Altair-RADIOSS solver, such as high-velocity explosions, explosive effects, and drop and impact analyses. All of the simulations above involve significant plastic deformation. Numerical modelling of refill FSSW involves large plastic deformations and steep temperature gradients, presenting difficulty in non-linear material behaviour. Therefore, Altair-RADIOSS is used for modelling the refill FSSW process.

2.1 Geometry and material model

CATIAv5 was used to model and assemble the geometries of the specimens, tool-set-clamping ring, shoulder and probe, and backing anvil, see Fig. 2.¹ The assembled geometry setup was then transferred to the Altair-RADIOSS. The material deformation is observed within the rotating tool's diameter and a narrow adjacent region. Additionally, the temperatures crucial in this process are those from the same region. Therefore, workpiece length, tool-set heights, and backing anvil thickness in this numerical model are reduced to speed up computation without affecting the model's accuracy. The tool-set heights are varied depending on the variant.

Solid-state joining procedures frequently employ the Johnson–Cook (JC) model constitutive law [19, 20, 22] because it considers the impact of temperatures, strain rates, and strain on flow stress, see Eq. (1).

$$\sigma_y = \left[A + B \left[\varepsilon^{pl} \right]^n \right] \left[1 + C \ln \left(\frac{\dot{\varepsilon}^{pl}}{\dot{\varepsilon}^0} \right) \right] \left[1 - \left[\frac{T - T_r}{T_m - T_r} \right]^m \right], \quad (1)$$

The material yield stress (σ_y) varies with temperatures (T_r —reference temperature, T_m —melting temperature), strain rate ($\dot{\varepsilon}^{pl}$ —plastic strain rate, $\dot{\varepsilon}^0$ —reference plastic strain rate), and equivalent plastic strain (ε^{pl}). The material constants are A (quasi-static yield strength), B (strain hardening), n (coefficient of strain hardening), m (coefficient of thermal softening), and C denotes the strengthening coefficient. The current model made use of the material properties and JC law's coefficients for AA7075-T6 that were reported in the prior study [33]. In Altair-RADIOSS, the material card MAT4 was used to define the JC material model. The efficiency of heat generation from strain is assumed to be 90%. The backing anvil and the tool-set are considered to be rigid.

¹ Note that the dimension of the shoulder, probe and clamping ring are varied depending on the variant.

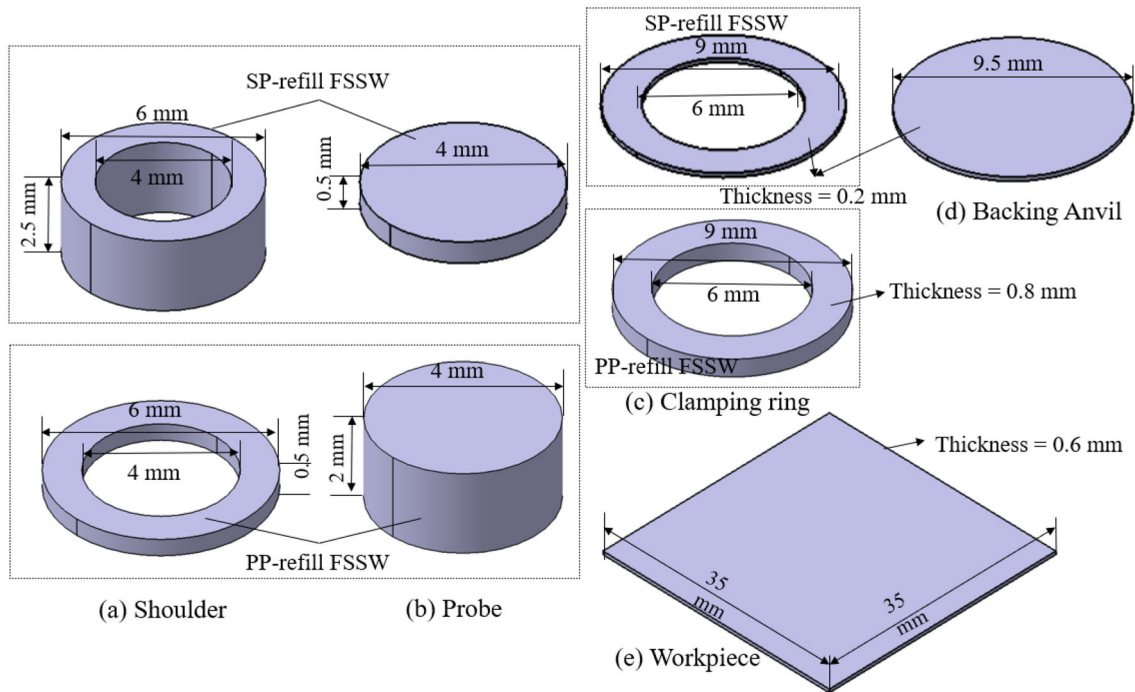


Fig. 2 Illustration of geometry used for the numerical models of SP-refill FSSW and PP-refill FSSW. **a** Shoulder; **b** Probe; **c** Clamping ring; **d** Backing Anvil

2.2 SPH Formulation

SPH can withstand extreme deformations that grid-based methods sometimes were unable to handle. The particle model in SPH makes it simple to precisely define material interactions and boundary conditions in a numerical model, which is a challenge in the grid-based method. Furthermore, the Lagrangian nature of this approach allows us to track field variables dynamically. The SPH technique was created to address the challenge of solving partial differential equations (PDE) in hydrodynamics that involve field variables such as density, velocity, energy, etc. The initial step in the SPH approach is to represent the PDE using a continuous integral representation of a function and its derivatives. In the second stage, for a collection of discrete points, the continuous SPH interpolation function is formulated. The integral approximation of a scalar function in space $\prod f(x)$ is given by:

$$\prod f(x) = \int_{\Omega} f(y)W(x - y, h)dy. \tag{2}$$

where the spatial distance between the interpolation point y and the function evaluation point x is represented by the kernel function $W(x - y, h)$, and where h is the smoothing length. The Dirac delta function property, support compactness, positivity, unity, and smoothness criteria should all be satisfied by the kernel function.

A set of particles at a position x_i ($i = 1, n$) is used in SPH to discretize a continuous domain of interest. The physical properties of each particle are distinct, including temperature, density, stress, and velocity. In addition to reflecting the field properties of the domain, these particles can be utilized for numerical interpolation. For the particles with mass m_i and density ρ_i , the smoothed approximation function and derivatives of the smoothed approximation function are given by:

$$\Pi_s f(x) = \sum_{i=1,n} \frac{m_i}{\rho_i} f(x_i)W(x - y, h) \tag{3}$$

$$\nabla f(x) = \sum_{i=1,n} \frac{m_i}{\rho_i} f(x_i)\nabla W(x - y, h) \tag{4}$$

The following kernel approximates the Gaussian kernel using cubic splines [34]; see Fig. 3.

$$r \leq h \rightarrow W(r, h) = \frac{3}{2\pi h^3} \left[\frac{2}{3} - \left(\frac{r}{h}\right)^2 + \left(\frac{r}{h}\right)^3 \right] \tag{5}$$

$$h \leq r \leq 2h \rightarrow W(r, h) = \frac{1}{4\pi h^3} \left(2 - \frac{r}{h} \right)^3 \tag{6}$$

$$2h \leq r \rightarrow W(r, h) = 0 \tag{7}$$

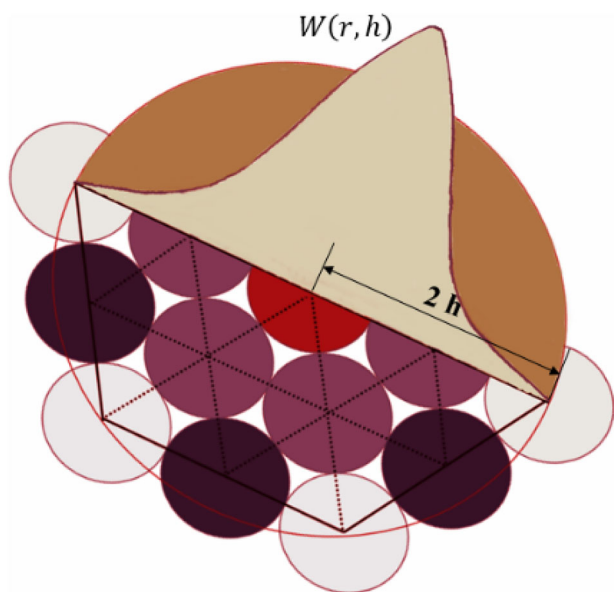


Fig. 3 Schematic representation of kernel, which approximates the Gaussian kernel using cubic splines

The governing equations for the conservation of mass, moment, and energy for solid deformation are expressed:

$$\frac{d\rho}{dt} + \nabla \cdot (\rho v) = 0 \tag{8}$$

$$\rho \frac{dv}{dt} = \nabla \cdot \bar{\sigma} \tag{9}$$

$$\rho C_p \frac{dT}{dt} = \nabla \cdot (k \nabla T) + \dot{q} \tag{10}$$

where the material’s density is denoted by ρ , time, the velocity field, and the stress tensor are all represented by the symbols t, v , and $\bar{\sigma}$, respectively. The internal heat generation rate per unit volume is denoted by \dot{q} , the specific heat capacity of the solid by C_p , temperature by T , and thermal conductivity by k . Each of the above three conservation Eqs. (8–10) can be stated in SPH form as given below:

$$\frac{d\rho_i}{dt} = \rho_i \sum_{j=1}^{N_i} \frac{m_j}{\rho_j} (v_i - v_j) \frac{\partial W_{ij}}{\partial x_i} \tag{11}$$

$$\frac{dv_i}{dt} = \sum_{j=1}^{N_i} m_j \left(\frac{P_i}{\rho_i^2} + \frac{P_j}{\rho_j^2} + \Pi_{ij} \right) \frac{\partial W_{ij}}{\partial x_i} \tag{12}$$

$$\frac{dT_i}{dt} = \frac{1}{\rho_i C_{pi}} \left[\sum_{j=1}^{N_i} \frac{m_j}{\rho_j} \frac{4k_i k_j}{k_i + k_j} \frac{(T_i - T_j)}{|x_i|^2} x_{ij} \frac{\partial W_{ij}}{\partial x_i} + \dot{q}_i \right] \tag{13}$$

where ρ_i, ρ_j are densities of the particles i and j , m_j is mass of particle j , $v_i - v_j$ is the relative velocity between

the particles i and j , W_{ij} is smoothing kernel for point i at point j , P_i, P_j are pressures of the particles i and j , Π_{ij} is the artificial viscosity term that accounts for viscosity effects between particles i and j , C_{pi} specific heat capacity of particle i , k_i, k_j are thermal conductivities of the particles i and j , respectively. $T_i - T_j$ is the difference of temperatures between particles i and j , and \dot{q}_i is internal heat generation rate per unit volume at particle position i .

2.3 Meshing, contact, and process controls

The top and bottom sheets were meshed/filled with 759,000 SPH particles. The pitch and smoothing length are 0.127 mm, and the particles are packed with simple cubic orientation. In the SP-refill FSSW variant, the shoulder was meshed with 20,996, the probe with 4241, the clamping ring with 4401, and the backing anvil with 8298 tetrahedral elements; see Fig. 4a. In the PP-refill FSSW variant, the shoulder was meshed with 8328, the probe with 11,017, and the clamping ring with 119,710 tetrahedral elements.

The refill FSSW process generates heat from frictional sliding energy at the workpiece-tool interface and mechanical strain from the workpiece’s plastic deformation. Consequently, accurate material deformation and heat generation require proper contact definition. A multi-usage node-to-surface type interface contact type (type 7 in Altair-RADIOSS) was created between the tool-set (main segment) and the workpiece (secondary nodes). This interface allows us to consider heat generation due to friction. The setup’s reference temperature/initial temperature is assumed to be 298 K. There is a limitation in the software to define heat transfer to the environment from SPH particles. Since the process duration is short, it was assumed that there is no heat transfer between the workpieces and the rigid tool-set. This gives the advantage of reducing the height of the backing anvil, tool-set, and computational cost. Friction between the spinning tool and the workpiece, as well as plastic deformation of the workpiece, are the primary sources of heat during refill FSSW. A Coulomb friction coefficient μ , which varies with the interface temperature (T_{int}), was employed in the simulation, see Fig. 5. Here, the interface temperature is the mean of temperatures of the interface’s main (T_m) and secondary sides (T_s).

SPH requires significantly more computing power than traditional mesh-based techniques because it additionally searches neighbouring particles to locate the kernel function and detect the node-to-surface contact. In order to minimize the computational time without sacrificing accuracy, the time step is extended to 1×10^{-6} s. This also increases the material density of the components in the model. The clamping ring and backing anvil movements are restricted in all degrees of freedom, and the probe and shoulder are constrained such that they can have rotation and translation about the vertical

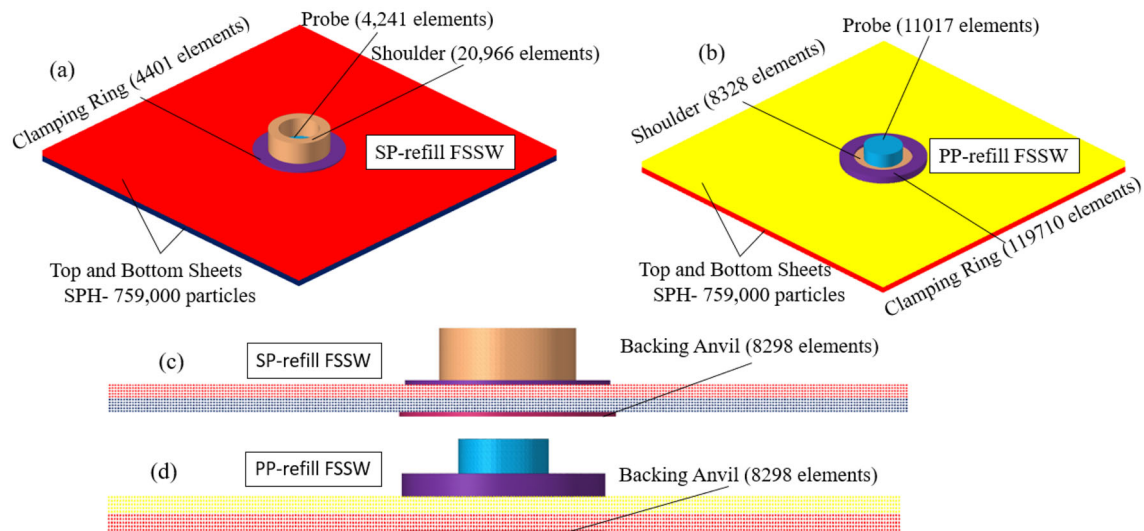


Fig. 4 Meshing details of the numerical model. **a** isometric view of SP-refill FSSW; **b** isometric view of PP-refill FSSW; **c** Side view of SP-refill FSSW; **d** Side view of PP-refill FSSW

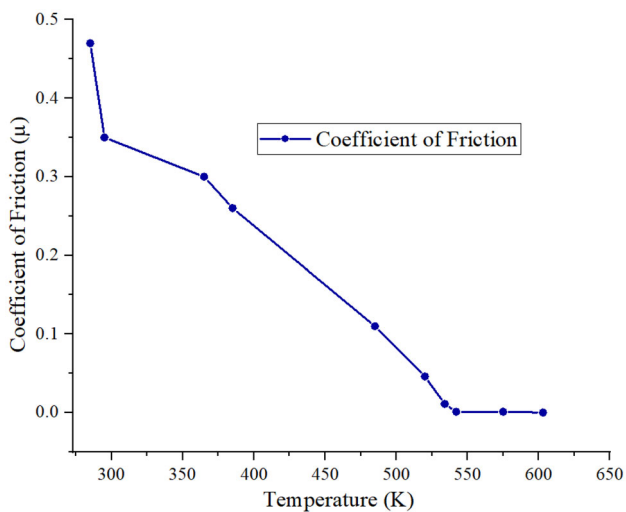


Fig. 5 Variation of coefficient of friction with interface temperature

axis. The probe and shoulder rotation speed (RS) and vertical movement are defined using imposed velocity and imposed displacement options, respectively. The following is a brief description of the simulation's stages in a 2.8 s process of SP-refill FSSW and PP-refill FSSW variants:

1. **Plunging stage:** During this stage, the rotating shoulder/probe (3000 rpm) descends at a plunge rate (PR) of 0.5 mm/s till a plunge depth (PD) of 0.7 mm. In SP-refill FSSW, the rotating probe (3000 rpm) with a PR (0.625 mm/s) moves upwards/opposite to the direction of the shoulder. In PP-refill FSSW, the rotating shoulder (3000 rpm) with a PR (0.4 mm/s) moves

upwards/opposite to the direction of the probe. The time for this stage is 1.4 s.

2. **Refilling stage:** Depending on the variant, the material is pushed into the specimen by having the shoulder/ probe reversing their directions while still moving at the PR's and rotating with the same RS as the previous stage. The time for this stage is also 1.4 s.

3 Results and discussion

At first, the SP-refill FSSW variant's computational model's accuracy in predicting thermal cycles was verified with the support of experimental temperatures from the literature [22]. The temperatures in the experiment were measured at the interface between the workpieces at locations L1 and L2 (L1-weld centre and L2–7.5 mm away from the weld centre, respectively). Predicting the specimen's temperature is crucial because it shows how well the heat generation has been modelled.

As shown in Fig. 6, the nodal temperature values are plotted at the locations L1 and L2. There is a good correlation between nodal temperatures from the simulation and experimental temperatures at the two locations. The highest nodal temperatures obtained from the simulation at the locations mentioned earlier are L1–772 K and L2–528 K. The peak temperatures from the literature recorded in the experiment are L1–768 K and L2–505 K. The variation in maximum temperatures measured experimentally at the weld centre (L1) and numerically predicted temperatures is 0.52%, and at L2 is

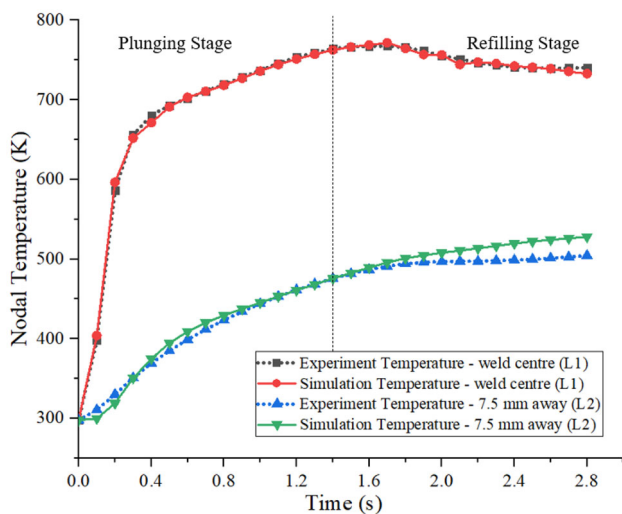


Fig. 6 Simulation nodal temperatures comparison with experimental temperatures at locations L1 and L2

4.5%. A sharp increase in temperature is seen up to 0.4 s initially during the plunging in the weld zone. The temperature then steadily increases until it reaches a peak at 1.7 s, gradually decreasing towards the end of the process. As you move out from the stir zone (SZ), the temperature is dropped. A sharp spike initially seen at L1 is no longer seen in L2, indicating that the temperature increased gradually throughout the procedure.

The temperatures and heat output are closely related, affecting how the material is stirred and softened during the refill FSSW process. Inadequate welding temperatures would prevent the proper flow of materials, resulting in a weak weld that lacks the desired surface finish. Figures 7a and 8a depict an axisymmetric temperature distribution about the weld centre at 1.7 s (maximum temperature) during the SP-refill FSSW and PP-refill FSSW simulation, respectively. Figure 7b–g and 8 b–g shows the temperatures in the SZ of SP-refill FSSW and PP-refill FSSW at various times of the process simulation, respectively. The maximum temperature from the SP-refill FSSW and PP-refill FSSW simulation is recorded to be 781 K and 780 K, respectively, at roughly 60% of the process duration. These peak temperatures correspond to about 80% of the base material's melting point (635 °C), a number frequently reported in FSW [35]. The temperature distribution shows that temperatures decrease with increasing distance from the weld centre in both variants. Both variants' SZ temperatures exceeded the alloy's solidus temperature (748 K/475 °C) [36]. The SZ material is softened more as the hardening precipitates ($MgZn_2$) in the base material dissolve rapidly, considering these higher temperatures in SZ [37]. Consequently, the material is better sheared and has enhanced movement as a result of this softening. Furthermore, the diffusion bonding between the top

and bottom sheets is strengthened at these high temperatures [36].

Temperature, strain, and strain rate are crucial factors in determining the final microstructure and grain size in refill FSSW. It is usually possible to recognize the characteristic zones from the micrograph from the experiments; see Fig. 9 [22]. However, it is challenging to determine the plastic strain that is locally undergone by the material to evolve into a particular microstructure experimentally. From the simulation results, the local plastic strain that the material underwent during the process can be measured. Figures 10 and 11 display plastic strain distribution at various stages of the SP-refill FSSW and PP-refill FSSW variants, respectively. The heat-affected zone (HAZ), in general, is the zone that is affected by temperature but not by any plastic strain. It can be determined from the plastic strain contour and temperature distribution in both variants. The SZ exhibits higher plastic strains, particularly in the vicinity of the shoulder (SAZ) in the SP-refill FSSW variant and under the probe (PAZ) in the PP-refill FSSW variant. The zone where moderate plastic strains are noticed and near the SZ is known as the thermo-mechanically affected zone (TMAZ). Moderate temperatures in TMAZ, as well as the mechanical movement of the material, are observed in the TMAZ. The TMAZ is a narrow region adjacent to the shoulder in SP-refill FSSW, while it is thicker around the probe in PP-refill FSSW. The final plastic strain contour at the SP-refill FSSW variant process end can be comparable to the microstructure from the experimental study [22]; see Fig. 10 g. From the SP-refill FSSW and PP-refill FSSW variant contours, it can be noticed that the plastic strain is symmetrical over the central axis of the tool, just like the thermal distribution. In the SP-refill FSSW variant, higher plastic strain is primarily seen under the shoulder, near the shoulder's inner edge during the plunging. The strain underneath the probe grew during refilling as the material was pressed down and slightly sheared outward by the probe's movement. While in the PP-refill FSSW variant, the higher plastic strain is observed under the probe during plunging and refilling. Therefore, the rotating shoulder has less influence in the refilling stage compared to the rotating probe in the refilling stage of the SP-refill FSSW variant. In the SP-refill FSSW variant, the area in the SAZ undergoes the most significant deformation due to shoulder plunging. Refined equiaxed grains are observed in the SZ due to dynamic recrystallization due to severe plastic strains and elevated temperatures. The dynamic recrystallization process relies on developing new grain boundaries, which can only occur in a strong plastic strain zone. The micrographs from the experimental studies of the SP-refill FSSW variant show that a much finer grain structure is observed in the SAZ when related to the probe-affected zone (PAZ) or centre of the weld, which is notably associated with severe plastic deformation in the SAZ than PAZ [10, 38, 39]. In the PP-refill FSSW

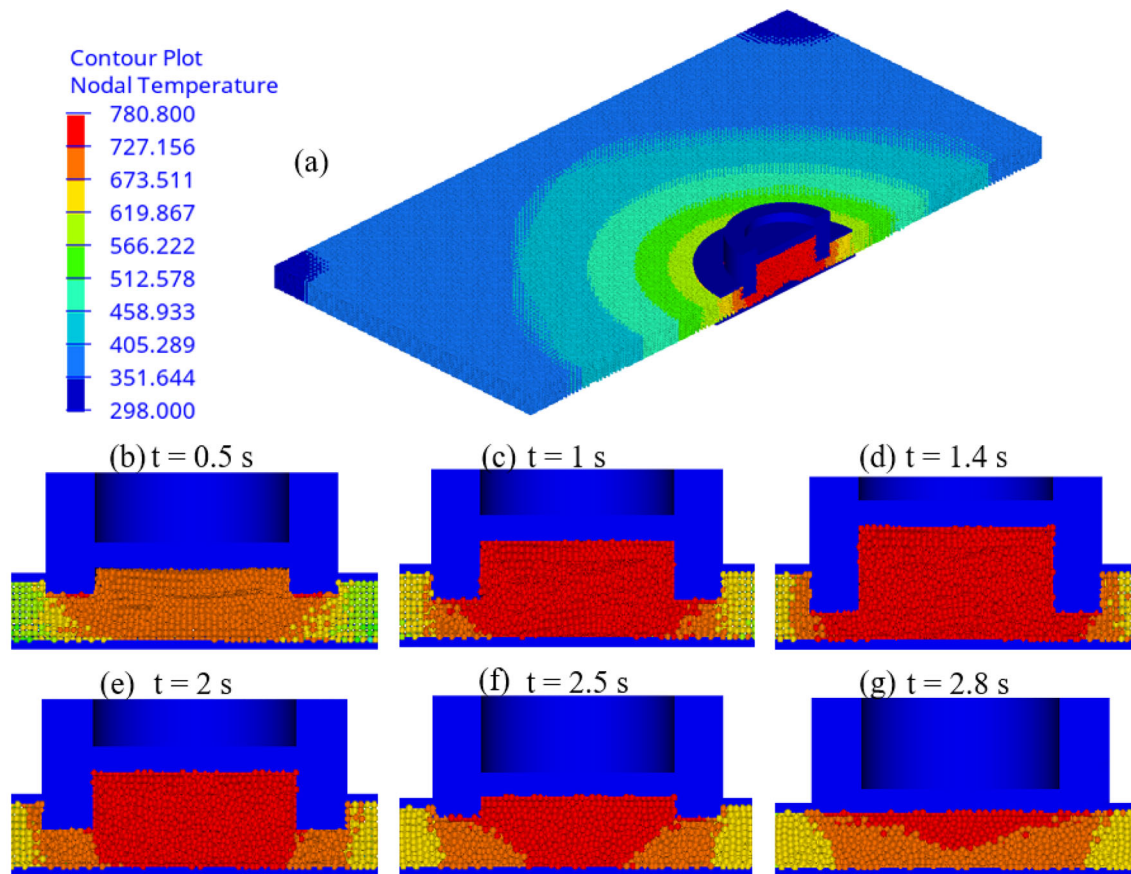


Fig. 7 Distribution of nodal temperatures during the SP-refill FSSW process. **a** $t = 1.7$ s; **b** $t = 0.5$ s; **c** $t = 1$ s; **d** $t = 1.4$ s; **e** $t = 2$ s; **f** $t = 2.5$ s; **g** $t = 2.8$ s

variant, the area in the PAZ undergoes the most significant deformation due to the plunging of the probe. The TMAZ area adjacent to the probe's outer edge is larger compared to the earlier variant. The TMAZ is known to be the softest among SZ, HAZ, and TMAZ as the thermal cycle in TMAZ is higher than HAZ and cannot reprecipitate like SZ [22, 40]. Therefore, this larger area of TMAZ in the PP-refill FSSW variant can reduce the weld strength.

The quality of the joint is highly dependent on the material flow during the refill FSSW process [13, 18]. Figures 12 and 13 depict displacement vectors during the process, providing an understanding of the material flow patterns in both variants. The material flow during the process primarily depends on the geometry of the spinning tools, RS, PD, and PR. The tool geometry, including the probe diameter and shoulder diameter, influences the size of the reservoir and the amount of material displaced during the plunging stage. The RS, PD, and PR determine the amount of heat generated and the amount of displaced and mixed material [21, 40]. During the shoulder-plunging, the material in the SZ is extruded upwards and inwards in the reservoir; see movement pattern (1) in Fig. 12a. The material in the SAZ is strongly sheared

outwards by the rotating shoulder; see movement pattern (2) in Fig. 12c. A portion of the material is pressed downward, particularly beneath the shoulder and close to the shoulder outer diameter; see movement pattern (3) in Fig. 12b. The material in the TMAZ, close to the outer edge of the shoulder, experiences vertical and lateral movements; see movement pattern (4) in Fig. 12b. During refilling, the material squeezed into the reservoir in the earlier stage is pressed downward by the probe; see movement pattern (5) in Fig. 12d. The material continued to shear outwards further during the refilling process. The material underneath the shoulder is pulled upward due to the combined action of the shoulder's upwards movement and the probe's downward movement; see movement pattern (6) in Fig. 12d. The material in the PAZ, close to the tool's central axis, has lower displacement compared to the material adjacent to the shoulder/SAZ. The highest displacement of material in the SAZ. When comparing the top and bottom sheets, the material displacements in the bottom sheet are lower.

Figure 13 a shows that the SZ material is ejected upwards and outwards into the reservoir as the probe plunges; see

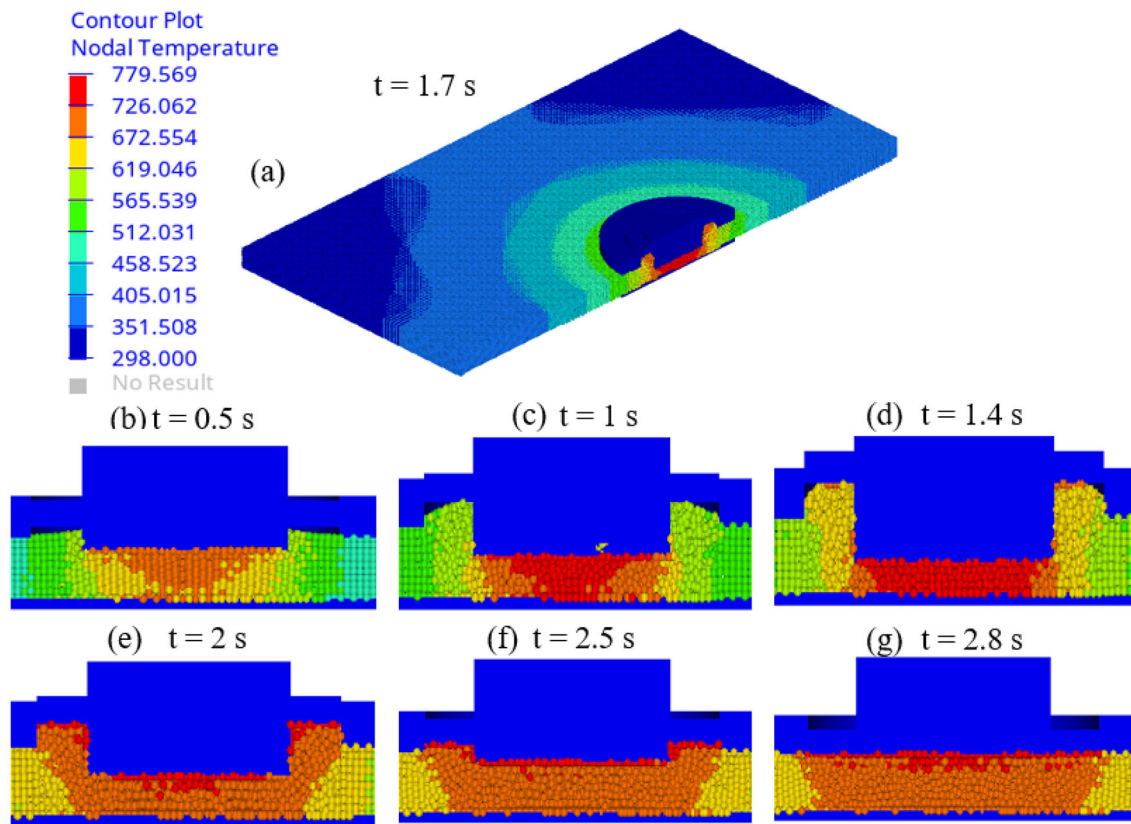


Fig. 8 Distribution of nodal temperatures during the PP-refill FSSW process. **a** $t = 1.7$ s; **b** $t = 0.5$ s; **c** $t = 1$ s; **d** $t = 1.4$ s; **e** $t = 2$ s; **f** $t = 2.5$ s; **g** $t = 2.8$ s

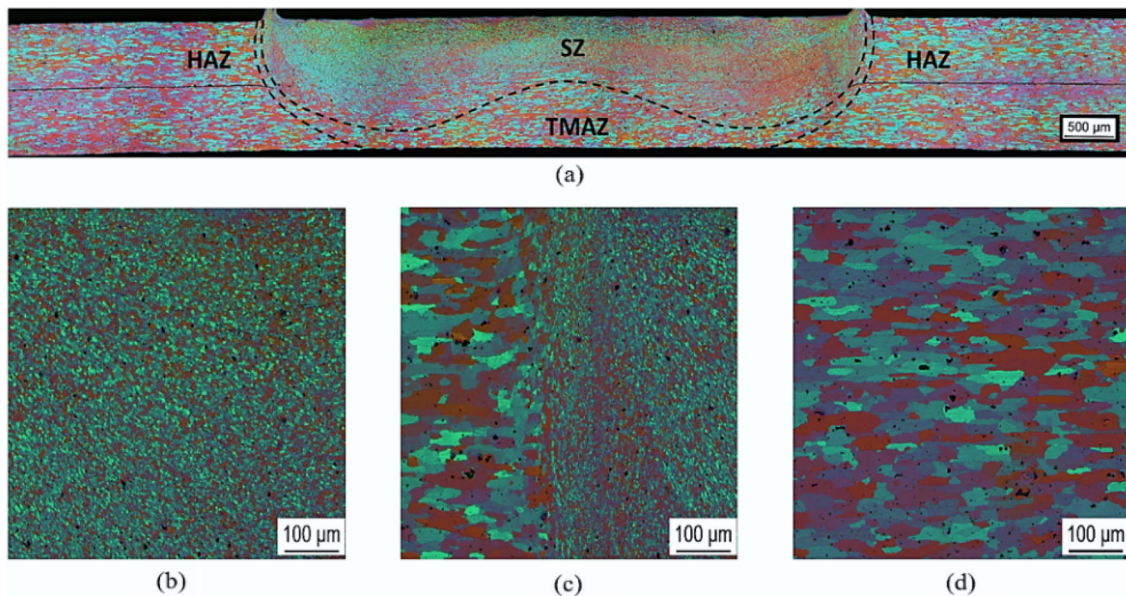


Fig. 9 Micrographs of the refill FSSW joint. **a** Joint's cross-section; **b** SZ; **c** junction between TMAZ and SZ; **d** Base Material [22]

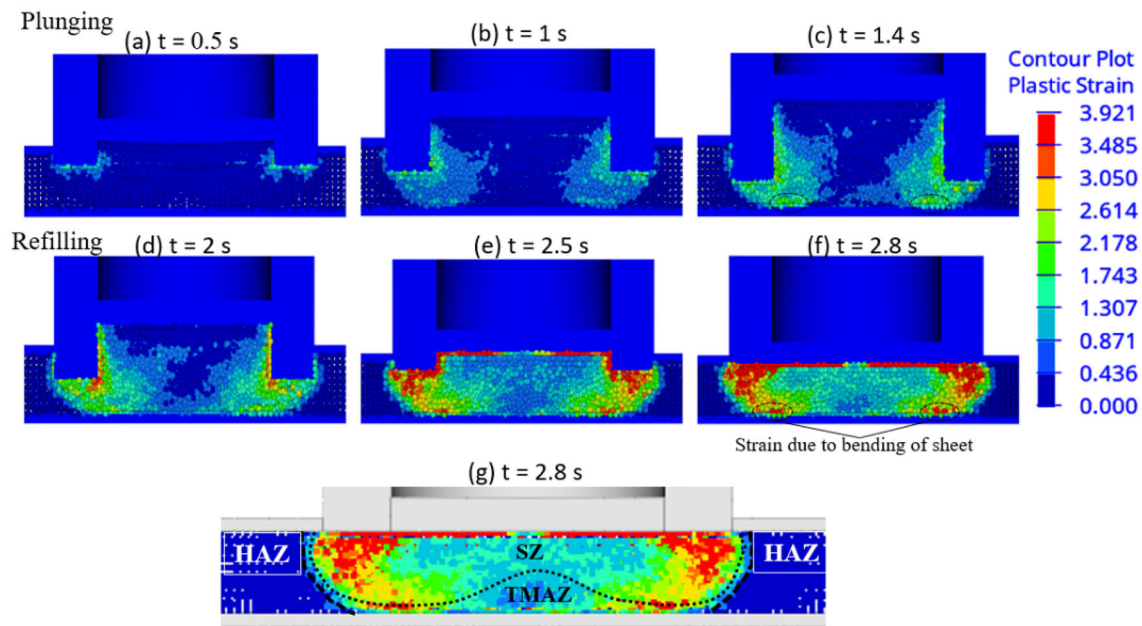


Fig. 10 Plastic strain distribution during the SP-refill FSSW process. **a** $t = 0.5$ s; **b** $t = 1$ s; **c** $t = 1.4$ s; **d** $t = 2$ s; **e** $t = 2.5$ s; **f** $t = 2.8$ s; **g** zone characterization at $t = 2.8$ s

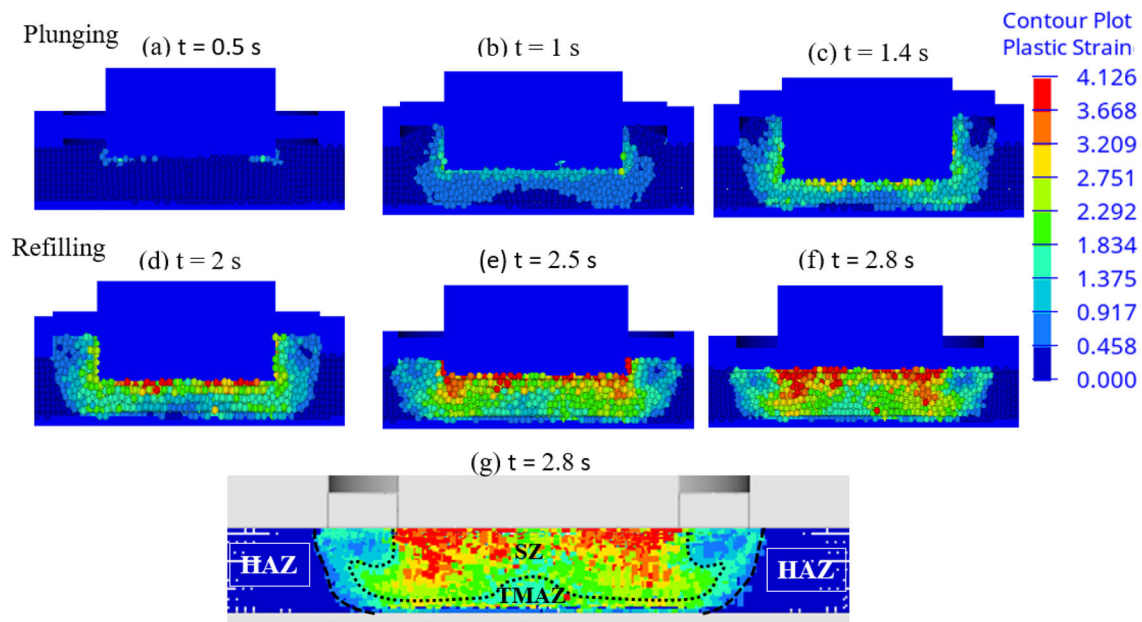


Fig. 11 Plastic strain distribution during the PP-refill FSSW process. **a** $t = 0.5$ s; **b** $t = 1$ s; **c** $t = 1.4$ s; **d** $t = 2$ s; **e** $t = 2.5$ s; **f** $t = 2.8$ s; **g** zone characterization at $t = 2.8$ s

movement pattern 1. See Fig. 13c, where the movement pattern (2) depicts the intense shearing of PAZ material outwards by the rotating probe, particularly at the outer edge of the probe. The motion pattern (3) in Fig. 13b is to observe how a portion of the material is pressed downward, significantly below the probe. As the material was being refilled, it continued to shear outward. Movement pattern (4) in Fig. 13d depicts the downward and inward motions experienced by the

TMAZ material towards the volume created by the probe's upward movement. See movement pattern (5) in Fig. 13d to illustrate how the upward motion of the probe works in tandem with the downward motion of the shoulder to lift the material beneath the probe. There is more movement in the material in the PAZ, near the probe's outer edge, than in the material in the shoulder/SAZ.

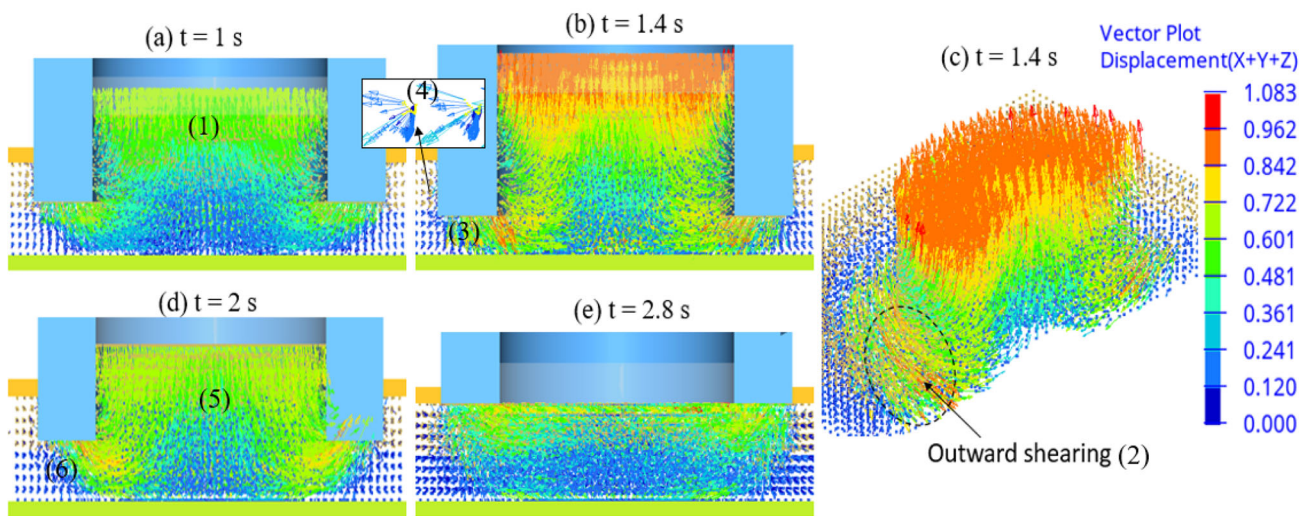


Fig. 12 Displacement vectors representing material flow patterns during the plunging and refilling stages of SP-refill FSSW

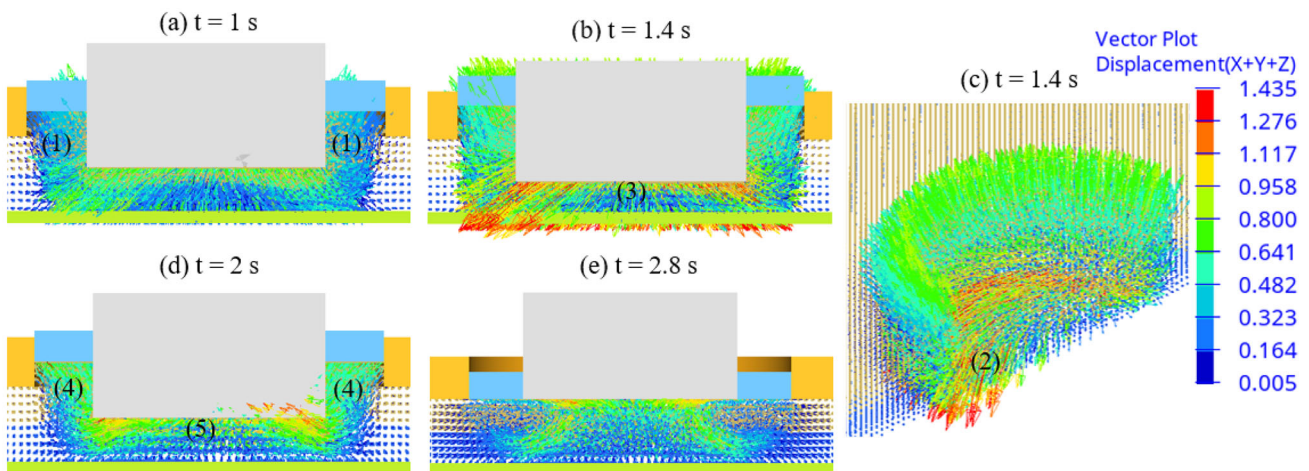


Fig. 13 Displacement vectors representing material flow patterns during the plunging and refilling stages of PP-refill FSSW

Figure 14 demonstrates the material movement during the SP-refill FSSW process. The material is squeezed into the volume (reservoir) formed by the tool’s action during the shoulder plunging. The bottom sheet material exhibits minimal movement at $t = 0.5$ s. The material movement in the bottom sheet marginally improved at $t = 1$ s. It can be noticed that the shoulder pierced into the bottom specimen at $t = 1.4$ s (at PD = 0.7 mm); see Fig. 14 c. The bending of the bottom sheet is seen at the end of the plunging; see Fig. 14c. The shape of the interface at the end of the plunging gives an ‘M’ shape, which agrees with the literature from earlier studies [13, 17, 41]. Figure 14d–e shows the refilling material flow. The revolving probe refills the weld zone with material from the reservoir. The probe pushes the collected material into the space created by the shoulder’s upward motion. This results in material intermixing in the SZ, which is critical in determining the joint characteristics. Because

of the intermixing, the joint’s strength may vary across its surface due to a change in microstructure and mechanical properties. Between the sheets, the material intermixing is noticed in the SAZ, similar to those reported in Refs. [21, 22]. A mechanical interlocking joining mechanism was created between the sheets as a result of material movement in the vertical direction, see Fig. 14 f. A flat weld is created after the refilling stage, as shown in Fig. 14 g, and defects like voids and underfill are not seen. During the process, a defect known as a “hook” can be formed at the edge of the weld. An upward bending ‘hook’ is formed as the PD in the process is greater than the upper sheet’s thickness [42]. The hook formation zone is highlighted in Fig. 14f. In the plunging stage, the interface under the probe is bent upwards, and under the shoulder is pushed downwards. The shoulder penetrates the bottom sheet at the end of plunging, and a portion of material close to the outer edge of the shoulder has upward

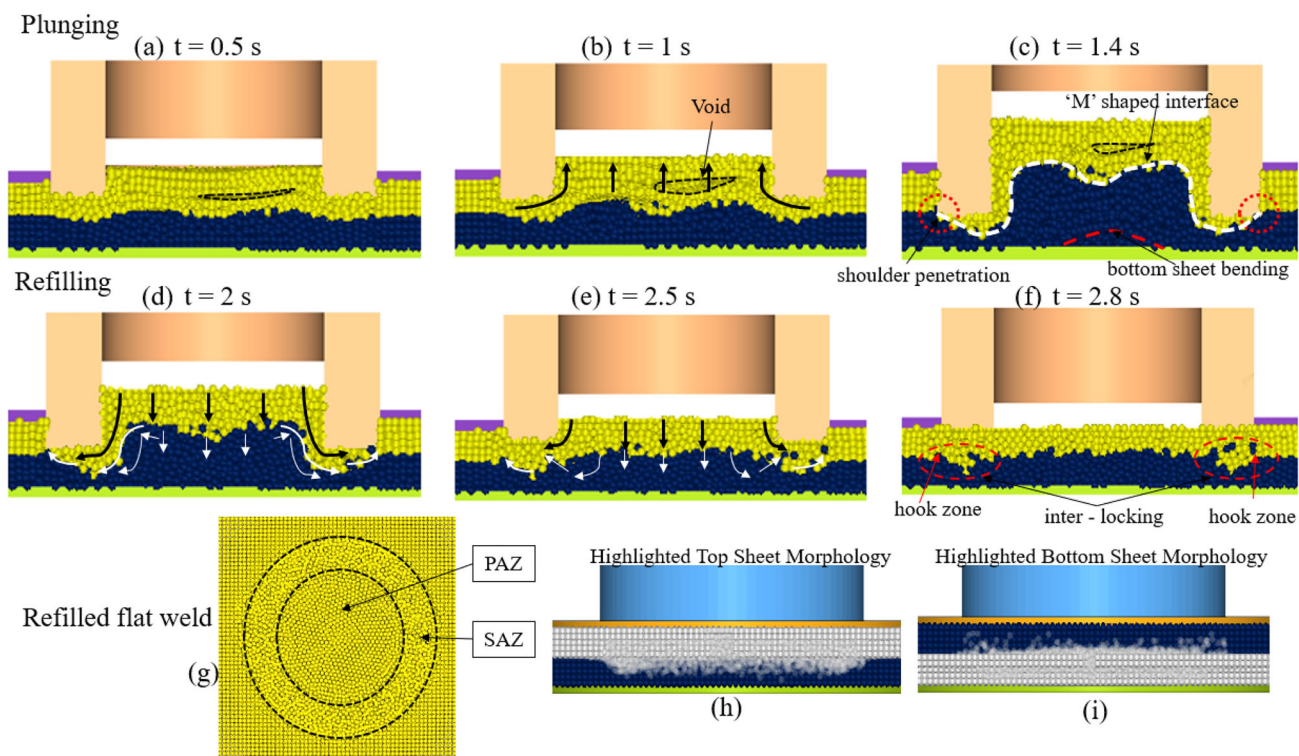


Fig. 14 Material flow illustration during the SP-refill FSSW process. **a–c** Plunging stage; **d–f** Refilling stage; **g** Refilled flat weld; **h** Highlighted top sheet morphology in the joint; **i** Highlighted bottom sheet morphology in the joint

movement, see Fig. 14c. During the refilling, the downward pushing of the interface by the probe results in the upward bending of the material away from the joint along with the material movement pattern (6), as discussed earlier, resulting in an upward bending hook. There is minimal material movement outside the shoulder’s diameter, which can also be seen from earlier plastic strain and displacement results. Most of the material movement that took place in the SZ is inside the shoulder peripheral region. The material movement outside the shoulder perimeter occurred in a relatively small TMAZ. The material flow directions, material flow while plunging, the shape of the interface at the end of plunging, and mechanical interlocking at the end of refilling are all consistent with the experimental findings documented in the literature [13, 17, 41].

Figure 15 depicts the material flow during the PP-refill FSSW process. The plasticized material is drawn into the reservoir made by the tool’s action during the plunging phase. At $t = 0.5$ s, there is slight movement in the bottom sheet. The material flow in the bottom sheet enhanced slightly at $t = 1$ s, and material adjacent to the probe’s outer edge started moving into the reservoir. Figure 15c shows that at $t = 1.4$ s, the probe penetrated the bottom specimen, and material in the reservoir was further moved upwards. The interface forms a ‘W’ shape at the end of the probe plunging. Figure 15d–e depicts the flow of refilling the softened material. When the

probe moves up, the shoulder presses the collected reservoir material into the volume created. This causes material mixing in the SZ, significantly defining the joint’s ultimate qualities; see Fig. 15f. An excellent material intermixing between the sheets is seen in PAZ. As shown in Fig. 14f and g, imperfections like voids and underfill are not visible following the refilling cycle, resulting in a flat weld in this variant. Although penetration and interface bend at the end of probe plunging like the SP-refill FSSW variant, hook formation is not seen in this variant. The reason is due to the inward pushing of the material during the refilling. Plastic strain and displacement findings from earlier in the process also show that the material outside the probe’s outer periphery and within the shoulder’s outer periphery has moderate movement (TMAZ). The TMAZ is a wider region outside the probe compared to the earlier variant. The size/volume of the weld is lesser compared to the SP-refill FSSW variant. The material mixing in the SZ is better in PP-refill FSSW. Therefore, the SP-refill FSSW is recommended over the PP-refill FSSW variant. The PP-refill FSSW with a bigger diameter probe and a shoulder with reduced thickness is recommended for joining the alclad specimens. This is due to its capability of better intermixing, and the alclad concentration, which weakens the joint, is better dispersed [14].

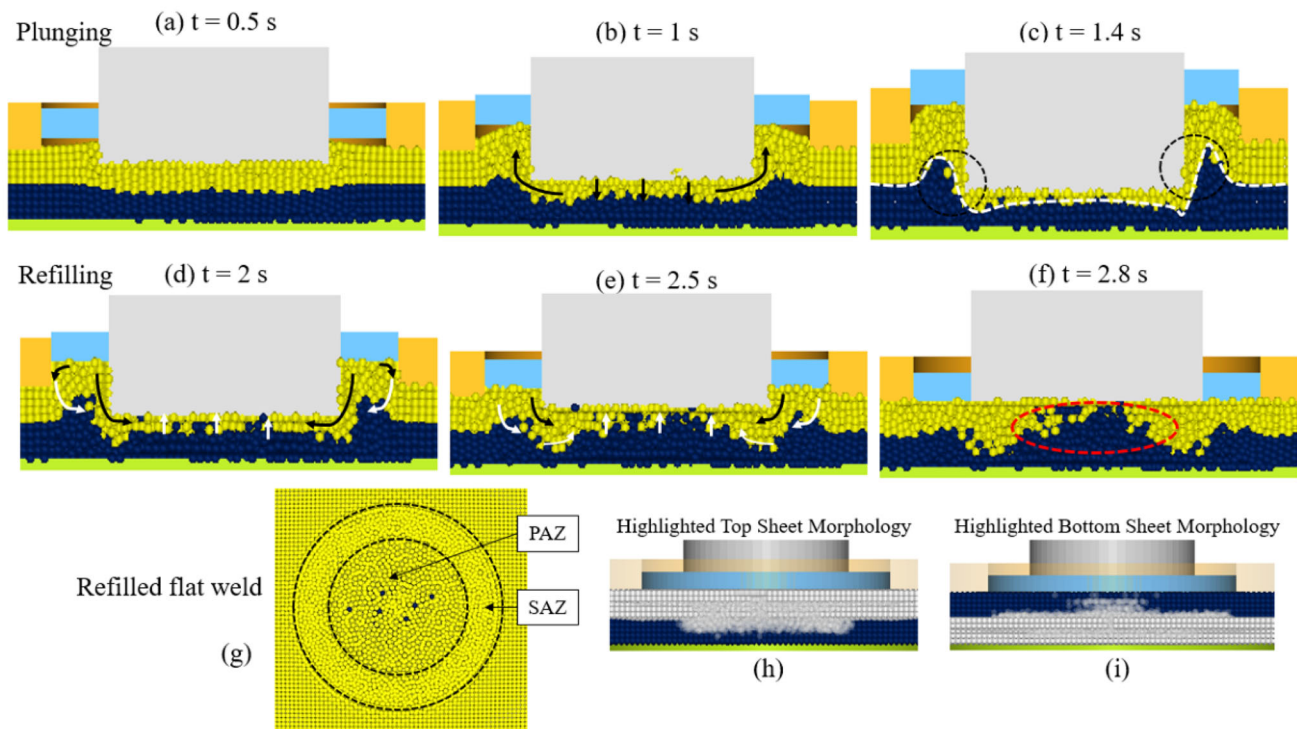


Fig. 15 Material flow illustration during the PP-refill FSSW process. **a–c** Plunging stage; **d–f** Refilling stage; **g** Refilled flat weld; **h** Highlighted top sheet morphology in the joint; **i** Highlighted bottom sheet morphology in the joint

4 Conclusions

A 3D numerical model with a mesh-free SPH approach was developed in this study to predict and understand complex thermo-mechanical conditions encountered during the refill FSSW process of SP-refill FSSW and PP-refill FSSW variants.

- The model is validated by comparing the experimental temperatures at two distinct locations in an SP-refill FSSW with those predicted numerically. The variation in maximum temperatures measured experimentally in the weld centre and numerically predicted temperatures for SP-refill FSSW is 0.52%.
- At around 60% of the process's total time (1.7 s), the process's maximum temperature is equivalent to roughly 80% of the material's melting point (635 °C) in both variants.
- Plastic strain contours show a symmetric distribution, and the maximum plastic strain is seen in the SAZ of the SZ for SP-refill FSSW and PAZ for the PP-refill FSSW variant.
- The numerical model is used to identify the SZ, TMAZ, and HAZ and the local plastic strains experienced by each zone in both variants.
- The hook formation during the SP-refill FSSW process is connected to the material flow patterns. The material

intermixing and defects are analyzed in both variants using the material flow patterns from the numerical models.

- The SP-refill FSSW is recommended for joining specimens with base alloy. The PP-refill FSSW, a larger diameter probe, and a thinner shoulder are recommended for joining alclad aluminium alloys.

Acknowledgements The authors acknowledge the funding they received from the Graduate Assistant Scheme at Universiti Teknologi PETRONAS and the help they received from Altair Engineering. Additionally, we appreciate the High-Performance Computing support for the simulations provided by the UTP-Altair Centre of Excellence for Applied Scientific Computing.

Author contributions VSRJ designed the methodology, conducted simulations and numerical analysis, and drafted and revised the manuscript. MA and NS provided resources and supervised the study, with MA also contributing to the methodology and manuscript review. CRM and EBW assisted with numerical modelling and manuscript review.

Declarations

Conflicts of interest The authors declare no conflict of interest.

References

1. Iwashita T (2003) Method and apparatus for joining. Patente, 6601751:B2

2. Nandan R, DebRoy T, Bhadeshia HKDH (2008) Recent advances in friction-stir welding - process, weldment structure and properties. *Prog Mater Sci* 53:980–1023. <https://doi.org/10.1016/j.pmatsci.2008.05.001>
3. Schilling C, Santos J dos (2004) Method and device for joining at least two adjoining work pieces by friction welding
4. Witthar K, Brown J, Burford D (2011) Swept FSSW in Aluminum Alloys through Sealants and Surface Treatments. In: *Friction Stir Welding and Processing VI*. John Wiley & Sons, Ltd, pp 417–424
5. Okamoto K, Hunt F, Hirano S (2005) Development of Friction Stir Welding Technique and Machine for Aluminum Sheet Metal Assembly- Friction Stir Welding of Aluminum for Automotive Applications (2) -. pp 2005–01–1254
6. Padhy GK, Wu CS, Gao S (2018) Friction stir based welding and processing technologies - processes, parameters, microstructures and applications: a review. *J Mater Sci Technol* 34:1–38. <https://doi.org/10.1016/j.jmst.2017.11.029>
7. Suresh S, Venkatesan K, Natarajan E, Rajesh S (2021) Performance analysis of nano silicon carbide reinforced swept friction stir spot weld joint in AA6061-T6 alloy. *SILICON* 13:3399–3412. <https://doi.org/10.1007/s12633-020-00751-4>
8. Balamurugan M, Gopi S, Mohan DG (2021) Influence of tool pin profiles on the filler added friction stir spot welded dissimilar aluminium alloy joints. *Mater Res Exp* 8(9):096531. <https://doi.org/10.1088/2053-1591/ac2771>
9. EsmerioMazzaferro JA, de Rosendo T, S, PetryMazzaferro CC, et al (2009) Preliminary study on the mechanical behavior of friction spot welds. *Soldag Inspecao* 14:238–247. <https://doi.org/10.1590/S0104-92242009000300007>
10. Shen Z, Chen Y, Hou JSC et al (2015) Influence of processing parameters on microstructure and mechanical performance of refill friction stir spot welded 7075–T6 aluminium alloy. *Sci Technol Weld Join* 20:48–57. <https://doi.org/10.1179/1362171814Y.0000000253>
11. Suhuddin UFH, Fischer V, Kostka A, dos Santos JF (2017) Microstructure evolution in refill friction stir spot weld of a dissimilar Al-Mg alloy to Zn-coated steel. *Sci Technol Weld Join* 22:658–665. <https://doi.org/10.1080/13621718.2017.1300744>
12. Shen Z, Chen J, Ding Y et al (2018) Role of interfacial reaction on the mechanical performance of Al/steel dissimilar refill friction stir spot welds. *Sci Technol Weld Join* 23:462–477. <https://doi.org/10.1080/13621718.2017.1414022>
13. Shen Z, Li WY, Ding Y et al (2020) Material flow during refill friction stir spot welded dissimilar Al alloys using a grooved tool. *J Manuf Process* 49:260–270. <https://doi.org/10.1016/j.jmappro.2019.11.029>
14. Cao JY, Zhang CC, Xing YF, Wang M (2020) Pin plunging reinforced refill friction stir spot welding of Alclad 2219 to 7075 alloy. *J Mater Process Technol* 284:116760. <https://doi.org/10.1016/j.jmatprotec.2020.116760>
15. Marode RV, Pedapati SR, Lemma TA, Awang M (2023) A review on numerical modelling techniques in friction stir processing: current and future perspective. *Arch Civ Mech Eng* 23:154. <https://doi.org/10.1007/s43452-023-00688-6>
16. Muci-Kuechler KH, Kalagara S, Arbegast WJ (2010) Simulation of a refill friction stir spot welding process using a fully coupled thermo-mechanical FEM model. *J Manuf Sci Eng-Trans Asme* 132:014503. <https://doi.org/10.1115/1.4000881>
17. Cao JY, Wang M, Kong L et al (2017) Numerical modeling and experimental investigation of material flow in friction spot welding of Al 6061–T6. *Int J Adv Manuf Technol* 89:2129–2139. <https://doi.org/10.1007/s00170-016-9247-3>
18. Ji S, Li Z, Wang Y et al (2017) Material flow behavior of refill friction stir spot welded LY12 Aluminum Alloy. *High Temp Mater Process* 36:495–504. <https://doi.org/10.1515/htmp-2015-0254>
19. Kubit A, Trzepiecinski T (2020) A fully coupled thermo-mechanical numerical modelling of the refill friction stir spot welding process in Alclad 7075–T6 aluminium alloy sheets. *Arch Civ Mech Eng* 20:117. <https://doi.org/10.1007/s43452-020-00127-w>
20. Zhang HF, Zhou L, Li GH et al (2021) Prediction and validation of temperature distribution and material flow during refill friction stir spot welding of AZ91D magnesium alloy. *Sci Technol Weld Join* 26:153–160. <https://doi.org/10.1080/13621718.2020.1864864>
21. Janga VSR, Awang M (2022) Influence of plunge depth on temperatures and material flow behavior in refill friction stir spot welding of thin AA7075-T6 sheets: a numerical study. *Metals* 12:927. <https://doi.org/10.3390/met12060927>
22. Janga VSR, Awang M, Yamin MF et al (2021) Experimental and numerical analysis of refill friction stir spot welding of thin AA7075-T6 sheets. *Materials* 14:7485. <https://doi.org/10.3390/ma14237485>
23. Berger E, Miles M, Curtis A et al (2022) 2D axisymmetric modeling of refill friction stir spot welding and experimental validation. *J Manuf Mater Process* 6:89. <https://doi.org/10.3390/jmmp6040089>
24. Raza SH, Mittnacht T, Diyoke G et al (2022) Modeling of temperature- and strain-driven intermetallic compound evolution in an Al–Mg system via a multiphase-field approach with application to refill friction stir spot welding. *J Mech Phys Solids* 169:105059. <https://doi.org/10.1016/j.jmps.2022.105059>
25. Gingold RA, Monaghan JJ (1977) Smoothed particle hydrodynamics: theory and application to non-spherical stars. *Mon Not R Astron Soc* 181:375–389. <https://doi.org/10.1093/mnras/181.3.375>
26. Lucy LB (1977) A numerical approach to the testing of the fission hypothesis. *Astron J* 82:1013–1024. <https://doi.org/10.1086/112164>
27. Tartakovskiy A, Grant G, Sun X, Khaleel M (2006) Modeling of Friction Stir Welding (FSW) Process with Smooth Particle Hydrodynamics (SPH). pp 2006–01–1394
28. Bhojwani S (2007) Smoothed particle hydrodynamics modeling of the friction stir welding process. *ETD Collect Univ Tex El Paso* 1–78
29. Pan W, Li D, Tartakovskiy AM et al (2013) A new smoothed particle hydrodynamics non-newtonian model for friction stir welding: process modeling and simulation of microstructure evolution in a magnesium alloy. *Int J Plast* 48:189–204. <https://doi.org/10.1016/j.ijplas.2013.02.013>
30. Fraser K, Kiss LI, St-Georges L, Drolet D (2018) Optimization of friction stir weld joint quality using a meshfree fully-coupled thermo-mechanics approach. *Metals* 8:101. <https://doi.org/10.3390/met8020101>
31. Ansari MA, Behnagh RA (2019) Numerical study of friction stir welding plunging phase using smoothed particle hydrodynamics. *Model Simul Mater Sci Eng* 27:055006. <https://doi.org/10.1088/1361-651X/ab1ca7>
32. Marode RV, Pedapati SR, Lemma TA, Janga VSR (2022) Thermo-mechanical modelling of friction stir processing of AZ91 alloy: using smoothed-particle hydrodynamics. *Lubricants* 10:355. <https://doi.org/10.3390/lubricants10120355>
33. Flores-Johnson EA, Shen L, Guaiamatsia I, Nguyen GD (2014) Numerical investigation of the impact behaviour of bioinspired nacre-like aluminium composite plates. *Compos Sci Technol* 96:13–22. <https://doi.org/10.1016/j.compscitech.2014.03.001>
34. Monaghan JJ (1992) Smoothed particle hydrodynamics. *Annu Rev Astron Astrophys* 30:543–574. <https://doi.org/10.1146/annurev.aa.30.090192.002551>
35. Tang W, Guo X, McClure JC et al (1998) Heat input and temperature distribution in friction stir welding. *J Mater Process Manuf Sci* 7:163–172. <https://doi.org/10.1106/55TF-PF2G-JBH2-1Q2B>

36. Gerlich A, Avramovic-Cingara G, North TH (2006) Stir zone microstructure and strain rate during Al 7075–T6 friction stir spot welding. *Metall Mater Trans A* 37:2773–2786. <https://doi.org/10.1007/BF02586110>
37. Starink MJ (2001) Effect of compositional variations on characteristics of coarse intermetallic particles in overaged 7000 aluminium alloys. *Mater Sci Technol* 17:1324–1328. <https://doi.org/10.1179/026708301101509449>
38. Zhao YQ, Liu HJ, Chen SX et al (2014) Effects of sleeve plunge depth on microstructures and mechanical properties of friction spot welded alclad 7B04-T74 aluminum alloy. *Mater Des* 62:40–46. <https://doi.org/10.1016/j.matdes.2014.05.012>
39. Tier MD, Rosendo TS, dos Santos JF et al (2013) The influence of refill FSSW parameters on the microstructure and shear strength of 5042 aluminium welds. *J Mater Process Technol* 213:997–1005. <https://doi.org/10.1016/j.jmatprotec.2012.12.009>
40. Janga VSR, Awang M, Pedapati SR (2023) A numerical study on the effect of tool speeds on temperatures and material flow behaviour in refill friction stir spot welding of thin AA7075-T6 sheets. *Materials* 16:3108. <https://doi.org/10.3390/ma16083108>
41. Shen J, Lage SBM, Suhuddin UFH et al (2018) Texture development and material flow behavior during refill friction stir spot welding of AlMgSc. *Metall Mater Trans A* 49:241–254. <https://doi.org/10.1007/s11661-017-4381-6>
42. Sun G-D, Zhou L, Zhang R-X et al (2020) Effect of sleeve plunge depth on interface/mechanical characteristics in refill friction stir spot welded joint. *Acta Metall Sin Engl Lett* 33:551. <https://doi.org/10.1007/s40195-019-00968-2>

Publisher's Note Springer Nature remains neutral with regard to jurisdictional claims in published maps and institutional affiliations.

Springer Nature or its licensor (e.g. a society or other partner) holds exclusive rights to this article under a publishing agreement with the author(s) or other rightsholder(s); author self-archiving of the accepted manuscript version of this article is solely governed by the terms of such publishing agreement and applicable law.